Int. J. Electrochem. Sci., 12 **(2017)** 11343 – 11352, doi: 10.20964/2017.12.32

International Journal of
ELECTROCHEMICAL
SCIENCE
www.electrochemsci.org

Carbon Nanotube Doped with Gaseous-phase Silica/Sulfur Composite as a Cathode Material for High-performance Lithium–Sulfur Batteries

Yafang Guo, Aihua Jiang[*]*, Meng Qi, Yongxuan Hou, Jianrong Xiao*

College of Science, Guilin University of Technology, Guilin 541004, PR China
[*]E-mail: jah@glut.edu.cn

Received: 10 September 2017 / *Accepted:* 19 October 2017 / *Published:* 12 November 2017

Despite its high theoretical specific capacity and energy density, lithium–sulfur battery (Li–S) can be practically used only when the shuttle effect and insulation property of elemental sulfur are addressed. In this regard, carbon nanotubes (CNTs) doped with gaseous-phase silica/sulfur composite ($GPSiO_2$-CNTs/S-*X*) at different mass ratios are synthesized through solid-state fusion method and used as cathode for Li–S cells. Results show that $GPSiO_2$-CNTs/S cathode with a mass ratio of 3:1:7 can maximize the duration of the discharge platform. In addition, a high initial discharge capacity of 1508 mAh g^{-1} is obtained at 0.1 C. The excellent properties of the $GPSiO_2$-CNT/S composite can be attributed to its special 3D structure, which facilitates the reutilization of the trapped active material and considerably improves the conductivity of sulfur cathode.

Keywords: lithium–sulfur batteries; cathode material; gaseous-phase silica; carbon nanotubes

1. INTRODUCTION

Lithium–sulfur (Li–S) batteries exhibit high specific capacity (1675 mAh g^{-1}), high energy density (2600 Wh kg^{-1}) [1-4], low cost, and environmental friendliness; these batteries are increasingly becoming one of the most promising energy storage in light of the increasing energy demand from numerous applications, such as electric vehicles and large-scale renewable energy storage [5-7].

However, the development of Li–S batteries is still plagued with problems, such as poor electronic conductivity of elemental sulfur [8-10], volume change due to different volume densities of Li_2S (1.67 g cm^{-3}) and S (2.03 g cm^{-3}) [11-15], and high solubility of sulfur polymer ion Sn^{2-} ($3 \leq n \leq 6$) in electrode reactions [15-19]. Among these problems, the poor conductivities of sulfur and shuttle

effect, which directly result in low utilization rate of active materials and short cyclic life, have attracted special attention. Considerable efforts, such as combining sulfur with different carbon matrices [13,20-22], metal oxides [23-25], and polymers [26-28], have been exerted to address these problems. Recently, the use of SiO_2 has been explored for its potential to improve Li–S cell performance [29-31]. Brennan et al. [29] synthesized SiO_2-coated sulfur partials through wet synthesis and added mildly reduced grapheme oxide to form an interconnected conductive network. They used this cathode to obtain high initial discharge capacity of more than 1400 mAh g^{-1} at 0.02 C and maintain 763.2 mAh g^{-1} after 50 cycles. Wei et al. [30] prepared graphene/S/SiO_2 composite through chemical oxidative method and obtained a specific capacity of approximately 696 mAh g^{-1} after 30 cycles at 0.1 C. Nevertheless, both methods are complex, and their electrochemical performance is not ideal. In our previous study [32], we discovered a facile method to synthesize a gaseous-phase silica ($GPSiO_2$)/S cathode, which possesses high initial discharge capacity and long cycle life. Nonetheless, this cathode also displays some limitations. In particular, the insulation and general structure of $GPSiO_2$/S cannot improve the electron conductivity of Li–S cells. They also cannot effectively inhibit the shuttle effect. Thus, introducing conductive materials to the $GPSiO_2$/S composite is remarkably important. Given their excellent electrical conductivity and special tubular structure, multiwalled carbon nanotubes (CNTs) have attracted considerable attention; these materials have been used as an additive to improve the electronic conductivity of sulfur cathode [33-35].

In the present study, CNTs doped with $GPSiO_2$/sulfur composite ($GPSiO_2$-CNTs/S-*X*) are fabricated and used as cathode for Li–S cells. The $GPSiO_2$-CNT/S composites with different weight ratios of CNTs are prepared by melting and recrystallization of sulfur during heat treatment. $GPSiO_2$ and CNT contribute to the high specific capacity and excellent superior rate capability and energy density of Li–S cells.

2. EXPERIMENTAL SECTION

2.1 Preparation of $GPSiO_2$-CNTs/S-X composite

According to our previous study, $GPSiO_2$/S cathode with a mass ratio of 3:7 displays excellent performance [32]. Thus, this cathode was used in the present study. Different mass ratios of CNTs were used in the cathode to form $GPSiO_2$-CNT/S-*X* composites, where *X* represents the proportion of CNTs in the composite. First, pure sulfur, CNT, and gaseous-phase silica were ground together; the weight ratio of $GPSiO_2$:CNT:S was 3:0.5:7. Subsequently, the mixture was transferred into a 25 mL stainless steel autoclave. Second, we placed the autoclave in a glove box (Lab2000, Etelux, Beijing, China) filled with Ar gas for 30 min to remove residual air, thereby preventing the S oxidation at high temperatures. Finally, the autoclave was heated at 155 °C for 8 h. After cooling to room temperature, the $GPSiO_2$-CNT/S composites were obtained and marked as $GPSiO_2$-CNTs/S-0.5. The $GPSiO_2$-CNTs/S-*X* (*X* = 1, 2) composites were prepared similarly for comparison. A schematic illustration of the solid-state fusion process of $GPSiO_2$-CNTs/S is shown in Fig. 1.

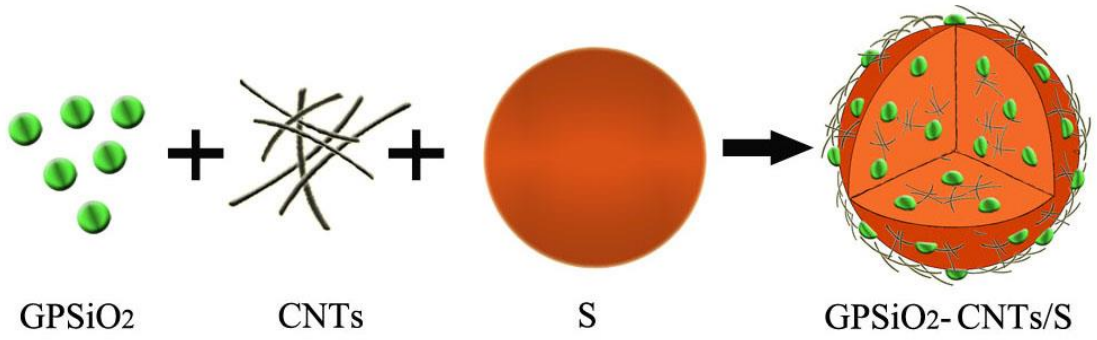

Figure 1. A schematic illustration of the solid-state fusion process of carbon nanotubes (CNTs) doped with gaseous-phase silica/sulfur ($GPSiO_2$-CNT/S) composites

2.2 Coin cell assembly

The cathode was prepared by uniformly mixing 70 wt.% of the active material ($GPSiO_2$-CNTs/S-*X*) with 20 wt.% of acetylene black (Taiyuan, China) and 10 wt.% of polyvinylidenefluoride (HSV900, Taiyuan, China) binder in *N*-methyl-2-pyrrolidone (AR, Tianjin, China). The mixture was subsequently pasted on an aluminum foil. The working cathode was obtained after drying at 60 °C in a vacuum oven overnight. CR2025-type coin cells were assembled with the cathode, pure lithium foil, and Celgard 2400 separator inside an argon glove box. The electrolyte was lithium bis(trifluoromethansulfonyl)-imide (1 M) in 1,2-dimethoxyethane and 1,3-dioxolane (1:1, vol.%) with 1 wt.% $LiNO_3$. All the cells were left to stand for 12 h before testing.

2.3 Material characterization

Phase and structure analyses were conducted through X-ray diffraction (XRD; CuKα radiation λ = 0.15418 nm, MiniFlex600) from 10° to 90°. Thermogravimetric (TG) analysis of $GPSiO_2$-CNTs/S-*X* was performed with TG/DTA 6300 to obtain the sulfur content in the composite. Sample morphology was determined with a scanning electron microscope (SEM, HitachiS-4800).

2.4 Electrochemical measurements

The charge/discharge cycle performance tests of the Li–S cells were carried out using a LAND Cell Test System (CT2001, Wuhan, China) with a voltage window of 1.5–2.8 V. Cyclic voltammetry (CV) and the electrochemical impedance spectrum (EIS) of cells were obtained using an electrochemical working station (CHI750E, Shanghai, China) with a scanning window of 1.0–3.0 V at a scan rate of 0.1 mVs^{-1}. The impedance test frequency window ranged from 0.01 Hz to 100 KHz with a voltage amplitude of 5 mV.

3. RESULTS AND DISCUSSION

3.1 Material characterization

The XRD patterns of pure sulfur and $GPSiO_2$-CNTs/S-*X* composites are illustrated in Fig. 2. Two high-intensity diffraction peaks are detected in the diffraction pattern of pure sulfur at 2θ of 23° and 28°; these peaks represent the orthorhombic structure of S_8. The diffraction peaks of $GPSiO_2$-CNTs/S-*X* are almost the same as that of the S peak. Nevertheless, the diffraction peak intensity decreases at increased CNT content, thereby indicating the homogeneous dispersion of pure sulfur in the pores of $GPSiO_2$ and CNTs during heat treatment.

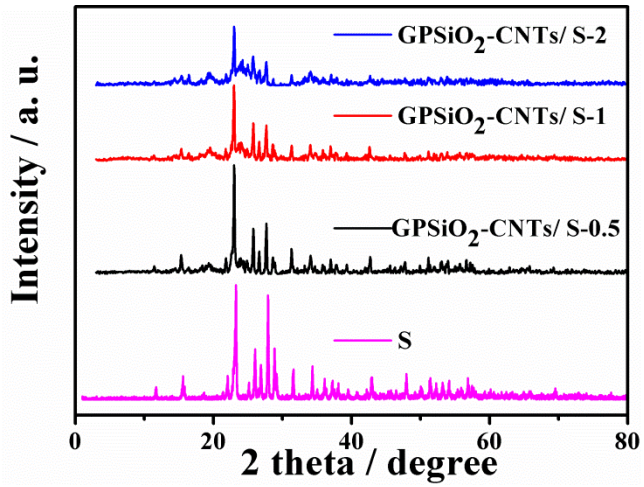

Figure 2. XRD patterns of pristine sulfur and $GPSiO_2$-CNTs/S-*X* (*X*=0.5, 1, 2) composites

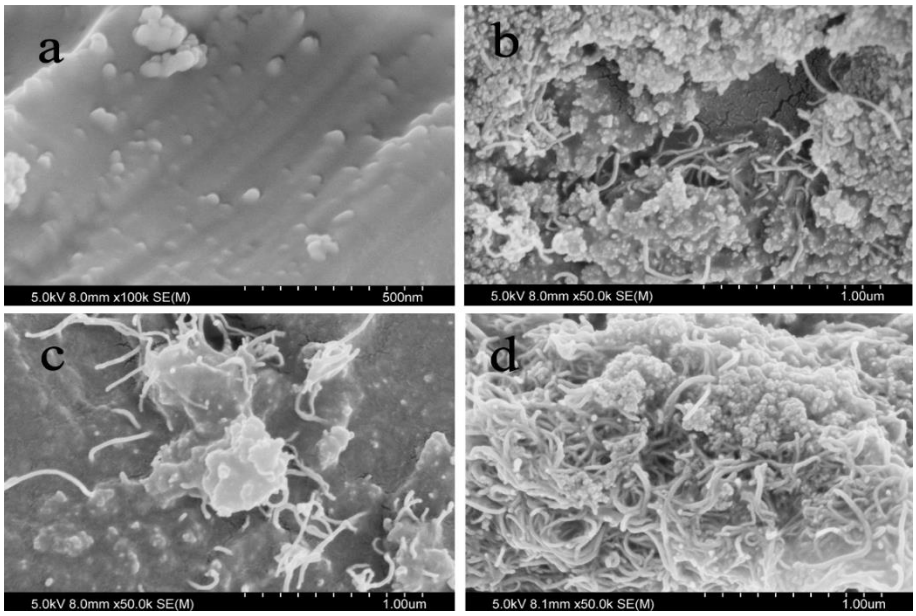

Figure 3. SEM images of the $GPSiO_2$/S (a), $GPSiO_2$-CNTs/S-0.5 (b), $GPSiO_2$-CNTs/S-1 (c), $GPSiO_2$-CNTs/S-2 composites (d).

The morphology and structure of $GPSiO_2$/S and $GPSiO_2$-CNTs/S-*X* were characterized through SEM measurements, as shown in Fig. 3. Figure 3a shows the morphology of the $GPSiO_2$/S surface at high magnification, and the uniformly projected particles are $GPSiO_2$. Figure 3b depicts the $GPSiO_2$-CNTs/S-0.5 structure, which exhibits a poor contact between $GPSiO_2$ and CNTs because of low CNT content. This phenomenon is significantly improved in Figs. 3c and 3d. As shown in Fig. 3c, CNTs run through sulfur and $GPSiO_2$, which enables the formation of a 3D structure. This structure enhances the electron transport properties of the composite. However, when the composite shows considerably high CNT content, the $GPSiO_2$ and CNTs agglomerate on the surface of sulfur (Fig. 3d), which results in unsatisfactory 3D structure.

TG measurement was conducted in Ar atmosphere to determine the S contents in the $GPSiO_2$-CNT/S-*X* composites. Measurement results are shown in Fig. 4. Sulfur completely loses its weight when heated to 270 °C, whereas the $GPSiO_2$-CNT composites maintain their initial weights. The S contents in the $GPSiO_2$-CNT/S-*X* composites are 66 wt.%, 64 wt.%, and 60 wt.% at *X* of 0.5, 1, and 2, respectively.

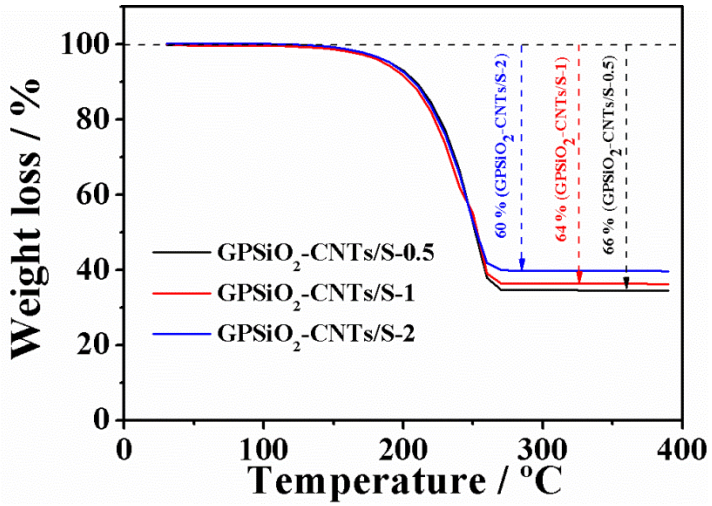

Figure 4. TGA analysis of the $GPSiO_2$-CNTs/S-*X* (*X*=0.5, 1, 2) composites

3.2 Electrochemical performance

Figure 5 illustrates the CV curves of the $GPSiO_2$-CNT/S-*X* composites. Two reduction peaks and one oxidation peak are shown in each circle. In addition, the reduction peak at 2.3 V originates from the transformation of S_8 into S_n^{2-}, and the reduction peak at 2.0 V develops from the transformation of S_4^{2-} into S^{2-} [34]. In the second scan, the two reduction peaks of $GPSiO_2$-CNTs/S-*X* move slightly to a high potential, and the oxidation peak also shifted, which suggested the formation of solid electrolyte interphase membrane on the cathode [36]. The overlapping CV curves in Fig. 5b indicate that the battery cycle is more stable than those in Figs. 5a and 5c because of the excellent 3D structure and good electrical conductivity of $GPSiO_2$-CNTs/S-1 composite. Figure 5d shows that the voltage corresponding to the reduction peaks increases, and the oxidation peak reduces at increased CNT content. These results can be attributed to the poor conductivity of $GPSiO_2$/S, which causes

polarization in batteries. Therefore, adding CNTs can improve the electrochemical performance of Li–S batteries.

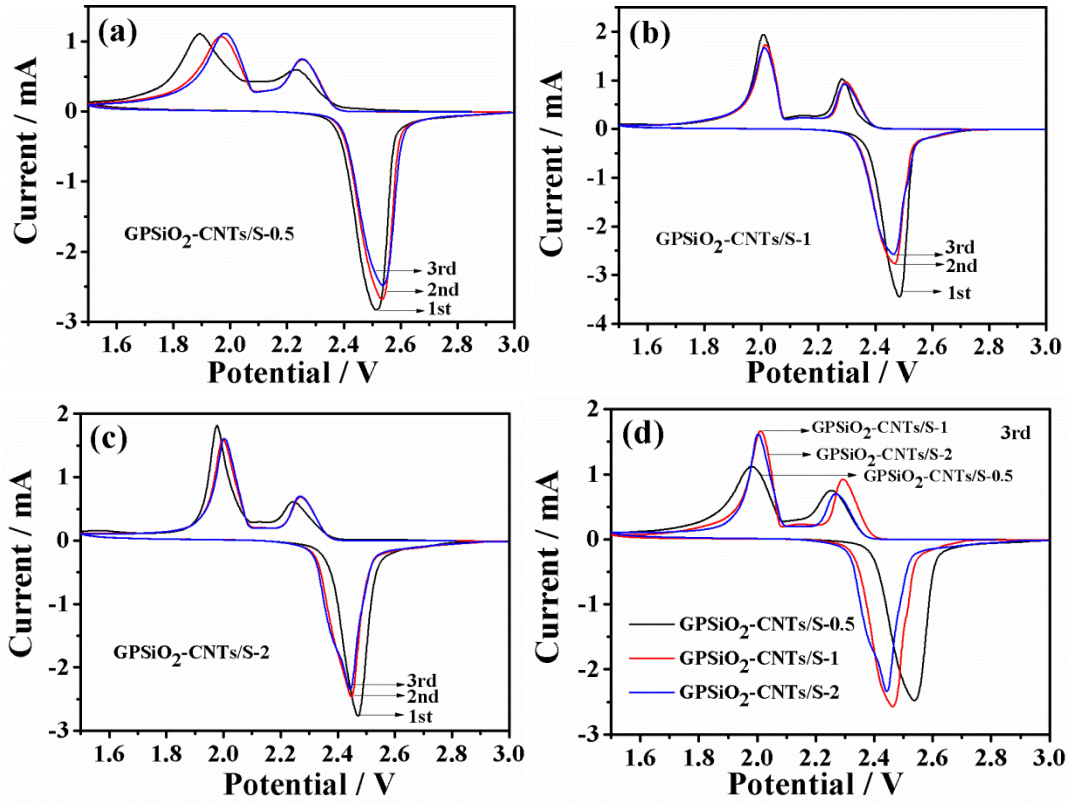

Figure 5. The cyclic voltammetry curves of the Li-S cells with the cathode of $GPSiO_2$-CNTs/S-0.5 (a), $GPSiO_2$-CNTs/S-1 (b), $GPSiO_2$-CNTs/S-2 (c), the CV curve in 3rd cycle (d) at a scanning rate of 0.1 mV s^{-1}.

Figure 6a displays the initial discharge performance of cells with different electrodes at a current density of 0.1 C (1 C = 1675 mAh g^{-1}) between 1.5 V and 2.8 V. The discharge profile of $GPSiO_2$-CNTs/S-*X* cathode shows two separate plateaus, which indicated that two reduction reactions occur. The upper and lower platforms are approximately at 2.3 and 2.1 V, and they correspond to the first reduction of S_8 to S_n^{2-} ($5 \leq n \leq 8$) and second reduction of S_n^{2-} ($5 \leq n \leq 8$) to S^{2-}/S_2^{2-}, respectively [37]. Table 1 shows that the initial specific capacities of $GPSiO_2$-CNTs/S-0.5, $GPSiO_2$-CNTs/S-1, and $GPSiO_2$-CNTs/S-2 at 0.1 C reach approximately 1361, 1508, and 1546 mAh g^{-1}, respectively. Although the initial specific capacity of $GPSiO_2$-CNTs/S-2 contributes the most to high CNT content, its discharge speed is faster than that of $GPSiO_2$-CNTs/S-1. This result is attributed to that the special 3D structure of $GPSiO_2$-CNTs/S-1 can help inhibit the shuttle effect in Li–S cells and reduce the loss of active substances.

The cycle performance and coulombic efficiency of the $GPSiO_2$-CNTs/S-*X* cathode at 0.1 C are demonstrated in Fig. 6b. After 100 cycles, the discharge specific capacities of the $GPSiO_2$-CNTs/S-0.5, $GPSiO_2$-CNTs/S-1, and $GPSiO_2$-CNTs/S-2 are 613, 788, and 706 mAh g^{-1}, respectively. Additionally, the coulombic efficiency of the different cathodes is more than 99%. The discharge specific capacities of the $GPSiO_2$-CNTs/S-1 are also much higher than that of the $GPSiO_2$ cathode, which is

approximately 90% of sulfur utilization based on the theoretical capacity (1675 mAh g^{-1}); the capacity decay is also slow, as shown in Fig. 7a. These results revealed the excellent circulation ability of the cell with $GPSiO_2$-CNTs/S-1 cathode, the good inhibition of the shuttle effect, and the fast electron conduction and ion transport function of the 3D structure.

As listed in Table 2, the initial discharge capacity of the battery with the composite electrode of $GPSiO_2$-CNTs/S-1 is higher than that of the electrode of rGO/S/SiO_2 and graphene/S/SiO_2. Furthermore, the cycling ability of $GPSiO_2$-CNTs/S-1 is the most remarkable, thereby demonstrating its excellent electrochemical performance.

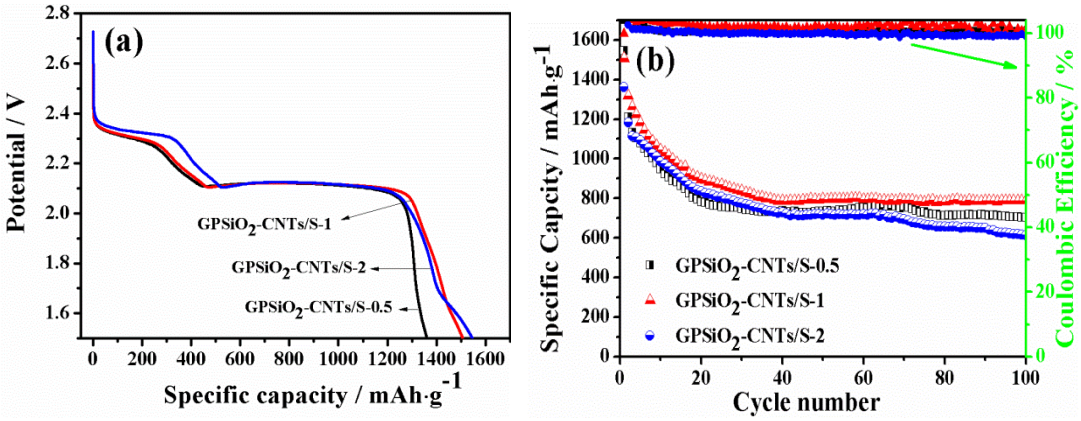

Figure 6. The first discharge/charge voltage profiles (a) and Cycle performances (Coulombic efficiency) of the $GPSiO_2$-CNTs/S-*X* (*X*=0.5, 1, 2) cathodes at 0.1 C (b).

Table 1. The specific capacity, Coulombic efficiency and sulfur utilization of the $GPSiO_2$-CNTs/S-*X* (*X*=0.5, 1, 2)

Cathode	Specific capacity (mAh g^{-1}) First cycle	100th cycle	sulfur utilization / %	Coulombic efficiency / %
$GPSiO_2$-CNTs/S-0.5	1361	613	81	100
$GPSiO_2$-CNTs/S-1	1508	788	90	100
$GPSiO_2$-CNTs/S-2	1546	706	92	99

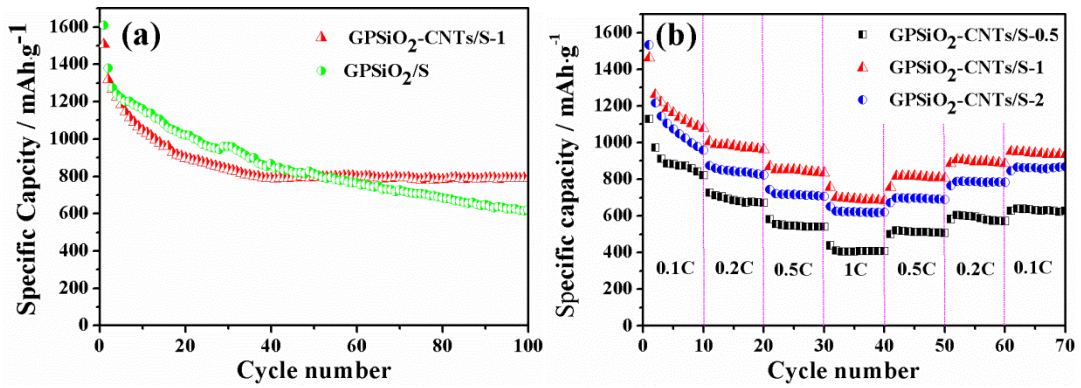

Figure 7. The cycle performances of cells with $GPSiO_2$-CNTs/S-1 cathode and the $GPSiO_2$/S cathode at 0.1C (a). The rate capacities of the cells with $GPSiO_2$-CNTs/S-*X* (*X*=0.5, 1, 2) cathodes (b).

Table 2. Cycling performance of the batteries with different composite electrode

Composite electrodes	Reference	Current density	Cycling performance/ mAh▪g^{-1}	
rGO/S/SiO_2	[29]	0.02C	1400 (before cycling)	763 (50 cycles)
graphene/S/SiO_2	[30]	0.1C		696 (30 cycles)
$GPSiO_2$/S	[32]	0.1C	1610 (before cycling)	814 (50 cycles)
$GPSiO_2$-CNTs/S-1		0.1C	1508 (before cycling)	788 100 cycles)

The rate capability of the electrodes is presented in Fig. 7b. All of the electrodes were tested with the following current densities: 0.1 → 0.2 → 0.5 → 1 → 0.5 → 0.2 → 0.1 C. After 70 cycles, the discharge capacities of $GPSiO_2$-CNTs/S-0.5, $GPSiO_2$-CNTs/S-1, and $GPSiO_2$-CNTs/S-2 are 626, 935, and 868 mAh g^{-1}, which correspond to the capacity retention rates of 56%, 64%, and 57%, respectively. The good reversibility of $GPSiO_2$-CNTs/S-1 cathode is attributed to the special 3D structure. This structure can serve as an elastic buffer and weaken the strain generated from the volume expansion of sulfur during the reduction process, which helps maintain a stable rate capability of Li–S cells.

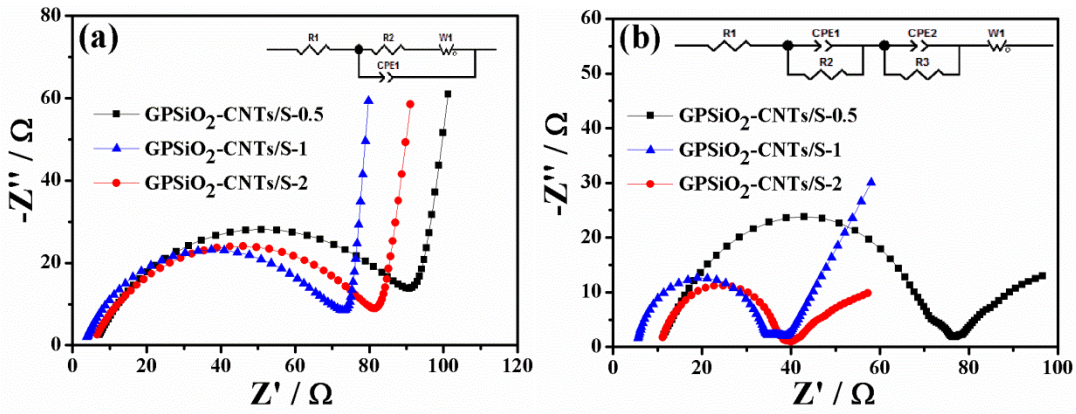

Figure 8. Electrochemical impedance spectrum (EIS) of the cells with $GPSiO_2$-CNTs/S-*X* (*X*=0.5, 1, 2) cathodes before (a) and after 10 cycles (b).

In addition, the EIS of different electrodes before and after cycles are examined in Fig. 8 at frequencies ranging from 0.01 Hz to 100 KHz. Z-view Software was used to fit an equivalent circuit (Fig. 8, inset). The EIS curves consist of a semicircle at high and medium frequencies; these curves correspond to the charge transfer resistance and an inclined line at low frequency, which is in accordance with Warburg impedance. A high-frequency intercept indicates ohmic resistance [23,38,39]. According to the equivalent circuit fitting, the charge transfer resistance of $GPSiO_2$-CNTs/S-1 is the lowest before and after the cycles. Given the excellent electrical conductivity and abundant holes of the $GPSiO_2$-CNTs/S-1 cathode material, active substance can be utilized. The Li–S cell performance can also be considerably improved.

4. CONCLUSIONS

$GPSiO_2$-CNTs/S-*X* (*X* = 0.5, 1, 2) composites were prepared to serve as cathodes of Li–S cells for the first time. Li–S cells with $GPSiO_2$-CNTs/S-1 cathode possess a high initial discharge capacity of 1508 mAh g^{-1}. The discharge capacity is maintained at 788 mAh g^{-1} after 100 cycles at a discharge current of 0.1 C. $GPSiO_2$-CNTs/S-1 is the most remarkable among the three composites. Moreover, the cells exhibit a long discharge platform and low impedance. The excellent electrochemical performance of $GPSiO_2$-CNTs/S-1 is attributed to the special 3D structure, which enhances the electronic conductivity and acts as an elastic buffer for polysulfide. Therefore, among the three synthesized composites, the $GPSiO_2$-CNTs/S-1 cathode possesses the most remarkable electrochemical performance for Li–S batteries.

ACKNOWLEDGEMENTS
The authors are grateful to the National Natural Science Foundation of China (Grant No. 11364011) and the Guangxi Natural Science Foundation (Grant No. 2015GXNSFAA139004).

COMPLIANCE WITH ETHICAL STANDARDS

CONFLICT OF INTEREST
The authors declare that there is no conflict of interests regarding the publication of this paper.

References

1. G. Hu, C. Xu, Z. Sun, S. Wang, H.M. Cheng, F. Li and W. Ren, *Adv Mater*, 28 (2016) 1603-1609.
2. M. Xiang, L. Yang, Y. Zheng, J. Huang, P. Jing, H. Wu, Y. Zhang and H. Liu, *J. Mater. Chem. A*, 5 (2017) 18020-18028.
3. X. Hong, J. Jin, T. Wu, Y. Lu, S. Zhang, C. Chen and Z. Wen, *J. Mater. Chem. A*, 5 (2017) 14775-14782.
4. M. Yu, A. Wang, F. Tian, H. Song, Y. Wang, C. Li, J.D. Hong and G. Shi, *Nanoscale*, 7 (2015) 5292-5298.
5. N. Liu, B. Huang, W. Wang, H. Shao, C. Li, H. Zhang, A. Wang, K. Yuan and Y. Huang, *ACS Appl Mater Inter*, 8 (2016) 16101-16107.
6. G. Zhou, L. Li, D.W. Wang, X.Y. Shan, S. Pei, F. Li and H.M. Cheng, *Adv Mater*, 27 (2015) 641-647.
7. C. Zu, Y.S. Su, Y. Fu and A. Manthiram, *Phys Chem Chem Phys*, 15 (2013) 2291-2297.
8. W. Cai, G. Li, F. He, L. Jin, B. Liu and Z. Li, *J Power Sources*, 283 (2015) 524-529.
9. S.-H. Chung and A. Manthiram, *Adv Funct Mater*, 24 (2014) 5299-5306.
10. M. Gu, J. Lee, Y. Kim, J.S. Kim, B.Y. Jang, K.T. Lee and B.-S. Kim, *RSC Adv.*, 4 (2014) 46940-46946.
11. D. Zheng, X. Zhang, J. Wang, D. Qu, X. Yang and D. Qu, *J Power Sources*, 301 (2016) 312-316.
12. D.H. Wang, X.H. Xia, D. Xie, X.Q. Niu, X. Ge, C.D. Gu, X.L. Wang and J.P. Tu, *J Power Sources*, 299 (2015) 293-300.
13. J. Zhang, H. Ye, Y. Yin and Y. Guo, *J Energy Chem*, 23 (2014) 308-314.
14. J. Balach, T. Jaumann, M. Klose, S. Oswald, J. Eckert and L. Giebeler, *Adv Funct Mater*, 25 (2015) 5285-5291.
15. J. Balach, H.K. Singh, S. Gomoll, T. Jaumann, M. Klose, S. Oswald, M. Richter, J. Eckert and L.

Giebeler, *ACS Appl Mater Inter*, 8 (2016) 14586-14595.
16. J. Xiao, H. Wang, Y. Hou and Y. Guo, *RSC Adv.*, 6 (2016) 38943-38949.
17. F. Nitze, K. Fossum, S. Xiong, A. Matic and A.E.C. Palmqvist, *J Power Sources*, 317 (2016) 112-119.
18. J. Conder, A. Forner-Cuenca, E.M. Gubler, L. Gubler, P. Novak and S. Trabesinger, *ACS Appl Mater Inter*, 8 (2016) 18822-18831.
19. J. Conder, S. Urbonaite, D. Streich, P. Novák and L. Gubler, *RSC Adv.*, 5 (2015) 79654-79660.
20. R. Sahore, L.P. Estevez, A. Ramanujapuram, F.J. DiSalvo and E.P. Giannelis, *J Power Sources*, 297 (2015) 188-194.
21. S. Lu, Y. Chen, J. Zhou, Z. Wang, X. Wu, J. Gu, X. Zhang, A. Pang, Z. Jiao and L. Jiang, *Sci Rep*, 6 (2016) 20445.
22. F.-l. Zhu, Z. Yang, J.-p. Zhao and X. Zhao, *New Carbon Mater*, 31 (2016) 199-204.
23. H. Tang, S. Yao, M. Jing, X. Wu, J. Hou, X. Qian, D. Rao, X. Shen, X. Xi and K. Xiao, *J Alloy Compd*, 650 (2015) 351-356.
24. T. An, D. Deng, M. Lei, Q.-H. Wu, Z. Tian, M. Zheng and Q. Dong, *J. Mater. Chem. A*, 4 (2016) 12858-12864.
25. X. Liu, Z. Shan, K. Zhu, J. Du, Q. Tang and J. Tian, *J Power Sources*, 274 (2015) 85-93.
26. B. Oschmann, J. Park, C. Kim, K. Char, Y.-E. Sung and R. Zentel, *Chem Mater*, 27 (2015) 7011-7017.
27. L. Qiu, S. Zhang, L. Zhang, M. Sun and W. Wang, *Electrochim Acta*, 55 (2010) 4632-4636.
28. L. Huang, J. Cheng, X. Li, D. Yuan, W. Ni, G. Qu, Q. Guan, Y. Zhang and B. Wang, *J. Mater. Chem. A*, 3 (2015) 4049-4057.
29. B. Campbell, J. Bell, H.H. Bay, Z. Favors, R. Ionescu, C.S. Ozkan and M. Ozkan, *Nanoscale*, 7 (2015) 7051-7055.
30. P. Wei, M. Fan, H. Chen, D. Chen, C. Li, K. Shu and C. Lv, *Int J Hydrogen Energ*, 41 (2016) 1819-1827.
31. S. Rehman, S. Guo and Y. Hou, *Adv Mater*, 28 (2016) 3167-3172.
32. Y. Hou, J. Xiao, Y. Guo, M. Qi, A. Jiang and Y. Li, *J Mater Sci-Mater El*, 28 (2017) 8901-8907.
33. J. Xiao, H. Wang, X. Li, Z. Wang, J. Ma and H. Zhao, *J Mater Sci-Mater El*, 26 (2015) 7895-7900.
34. Gong K, Du F and X. Z, *Science*, 323 (2009) 760-764.
35. W. Deng, A. Hu, X. Chen, S. Zhang, Q. Tang, Z. Liu, B. Fan and K. Xiao, *J Power Sources*, 322 (2016) 138-146.
36. J. Zheng, J. Tian, D. Wu, M. Gu, W. Xu, C. Wang, F. Gao, M.H. Engelhard, J.G. Zhang, J. Liu and J. Xiao, *Nano Lett*, 14 (2014) 2345-2352.
37. Z. Zhang, G. Wang, Y. Lai, J. Li, Z. Zhang and W. Chen, *J Power Sources*, 300 (2015) 157-163.
38. H. Li, L. Sun and G. Wang, *ACS Appl Mater Inter*, 8 (2016) 6061-6071.
39. J.-Q. Huang, Z.-L. Xu, S. Abouali, M. Akbari Garakani and J.-K. Kim, *Carbon*, 99 (2016) 624-632